POLITECNICO DI TORINO
Repository ISTITUZIONALE

Elastic and failure characterization of hydroxyapatite TPMS scaffolds using a combined approach of ultrasound, compression tests and micro-CT based numerical models

(Article begins on next page)

14 July 2025

Full length article

Elastic and failure characterization of hydroxyapatite TPMS scaffolds using a combined approach of ultrasound, compression tests and micro-CT based numerical models

Luca D'Andrea [a] [,1], Roberta Gabrieli [b,1], Lorenzo Milano [c], Luca Magagnin [c], Anna De Cet [a], Dario Alidoost [b,d], Martin Schwentenwein [e], Enrica Verné [b], Francesco Baino [b], Pasquale Vena [a],*

[a] Department of Chemistry, Materials and Chemical Engineering "Giulio Natta", Laboratory of Biological Structure Mechanics (LaBS) - Politecnico di Milano, Piazza Leonardo da Vinci 32, 20133, Milan, Italy
[b] Institute of Materials Physics and Engineering, Department of Applied Science and Technology - Politecnico di Torino, 10129, Turin, Italy
[c] Department of Chemistry, Materials and Chemical Engineering "Giulio Natta", Politecnico di Milano, via Mancinelli 7, 20131, Milan, Italy
[d] J-Tech Interdepartmental Research Centre, Politecnico di Torino, Corso Duca Degli Abruzzi 24, 10129, Turin, Italy
[e] Lithoz GmbH, Vienna, Austria

ARTICLE INFO

ABSTRACT

Hydroxyapatite is a widely used ceramic material for bone tissue engineering. For creating suitable scaffolds, reliable design and thorough characterization are essential. In this study, we designed and 3D printed three Triply Periodic Minimal Surface (TPMS) scaffold geometries using Vat Photopolymerization (VPP). We employed a combined experimental and numerical analysis approach to evaluate printing accuracy and its correlation with the mechanical properties of the scaffolds. Our findings indicate that VPP can print complex micro-architectures as those of the TPMS with thin wall thickness in the range of few hundreds of micrometers. Ultrasound waves and compression tests were conducted to determine the effective stiffness and strength of scaffolds, respectively. Finite Element Models were developed based on Computed micro-Tomography acquisitions to simulate the experimental compression tests, showing strong alignment with the experimental data. Among the tested TPMS geometries, the Diamond microstructures fail with the lowest specific strength, while the highest specific strength is shown by the I-graph and wrapped package-graph (IWP) scaffolds.

1. Introduction

Bone is a self-healing tissue but certain pathologies or traumatic events can lead to critical size bone defects, thus hindering the natural bone healing process. From a biological perspective, microstructured bioactive ceramic scaffolds have emerged as the preferred option among non-biologically derived materials due to their ability to promote osteogenesis [1], angiogenesis [2] and other beneficial properties (e.g., being engineered for controlled drug release in situ [3]).

Various factors must be simultaneously considered in the design of these scaffolds, including structural integrity, manufacturability, and permeability. Triply Periodic Minimal Surface (TPMS) geometries have been identified as a suitable choice, as they can meet all of these specifications with proper input parameters. Among the available additive

manufacturing techniques, Vat Photopolymerization (VPP) stands out as the most promising due to its ability to offer unbounded design possibilities and the best spatial resolution achievable to date [4].

Hydroxyapatite (HAP) TPMS scaffolds have been deeply studied with regard to their biological performance (e.g., [5–8]), while relatively little attention has been paid to the mechanical characterization. Indeed, TPMS VPP-produced scaffolds have already shown an early success in human clinical applications, but their use is still limited to anatomical sites with minimal load-bearing requirements, such as craniofacial defects [9]. Therefore, a comprehensive mechanical characterization of TPMS HAP scaffolds is needed to select mechanically compatible scaffolds for broader applications in orthopaedics and bone tissue engineering.

---

* Corresponding author.
E-mail addresses: luca.dandrea@polimi.it (L. D'Andrea), roberta.gabrieli@polito.it (R. Gabrieli), lorenzo.milano@polimi.it (L. Milano), luca.magagnin@polimi.it (L. Magagnin), anna.decet@polimi.it (A. De Cet), dario.alidoost@polito.it (D. Alidoost), mschwentenwein@lithoz.com (M. Schwentenwein), enrica.verne@polito.it (E. Verné), francesco.baino@polito.it (F. Baino), pasquale.vena@polimi.it (P. Vena).
[1] Equally contributed to the work.

A reliable prediction of the macroscopic elastic properties of a specific micro-architecture is essential in the design of the device. Extensive literature is available for this aim, using analytical approaches or finite element simulation on a representative volume element. In particular, the elastic modulus of lattice-like micro-architectures can be analyzed using beam mechanics and assuming deformation modes upon macroscopic compression strain [10,11]. On the other hand, beam-based finite element models can be applied on several microstructures (e.g., taking inspiration from crystallographic symmetries) to get the full elastic tensor, the Poisson's ratio in the Cartesian planes, as well as the Zener anisotropic index [12]. Furthermore, when the representative volume element is the repetitive unit of the lattice, periodic boundary conditions can be applied, saving computational time. Micro-architectures deriving from TPMS cannot be modeled as beams, thereby solid element numerical methods are needed for the prediction of the effective elastic properties. Also in this case, if a perfect periodicity of the structure can be identified, a unit repetitive cell can be used as a representative volume element. An upper bound of the macroscopic elastic modulus can be estimated by imposing displacement conditions with periodicity on the boundary which is macroscopically equivalent to a unit strain. If six different finite element simulations are carried out, each one corresponding to a single component of the unit strain, the full elastic tensor can be determined [13]. Smooth transitions among different TPMS can be introduced in a device with the purpose of expanding the available span of macroscopic elastic moduli [14]. Although the above-referenced works provide a suitable prediction of the effective elastic properties, they still rely on the knowledge of the material's properties (HAP in the present paper). It is worth mentioning that the latter are tightly dependent on the length scale and the specific manufacturing technique. In our previous work [15], we have shown the added value of testing small-scale samples having comparable size to the typical scaffold features (few hundreds of micrometers) and produced via the same method used for scaffold fabrication (both VPP and thermal treatment) in order to reliably reproduce the characteristics of scaffold struts and assess the microstructure and mechanical properties of the solid fraction accordingly. However, to the best of our knowledge, a similar approach has not been applied yet to TPMS ceramic scaffolds. Elastic modulus and strength of the materials are crucial in relation to the manufacturing process and certain manufacturing factors, such as the sintering temperature [16]. The size of the device's internal and external characteristics, however, must be accurately estimated to achieve reliable manufacturing capabilities because they greatly affect the device's overall stiffness and strength.

In order to advance the knowledge in the field of TPMS ceramic structures, which not only show promise in the biomedical field but can also be appealing in many other applications, this work has a twofold aim: (i) to determine the mechanical properties of HAP scaffolds with TPMS micro-architecture and 3D printed through the VPP technology with particular reference to the effective stiffness, compressive strength, and failure mechanisms; and (ii) to assess the production feasibility of these class of micro-architectures by means of the VPP process.

2. Materials and methods

2.1. Design and 3D printing of scaffolds

Three types of cylindrical TPMS scaffolds (i.e., Diamond, Gyroid and I-graph wrapped package-graph (IWP)) with two values of total porosity, have been designed starting from the analytical formulations provided by Ibrahimi et al. [17]. Binary three-dimensional image stacks have been created and lately converted to stl-files to be provided to the 3D printing equipment. The pixel scale has been set so to have a final diameter (D) of 8 mm and a height (H) of 16 mm (Fig. 1).

Two different sets of scaffolds have been prepared for each of the six types (three geometries and two porosities): one exhibiting two fully dense caps (thickness of 1 mm) at both ends of the cylinder,

and the other one without any fully dense cap. The samples with the caps have been used for macroscopic compression tests, while the samples without the caps have been used for ultrasound testing (see Section 2.4.1). The introduction of the bulk caps has been used to avoid the stress concentrations at the interface between the microstructure and the loading nose of the compression machine; this approach has been already documented in [18] where HAP samples were characterized. For each TPMS type, we created 30 scaffolds with caps for compression tests, 6 scaffolds without caps for: ultrasound testing (three samples), μCT imaging (one sample), XRD (one sample) and one additional sample was archived in the lab. The 36 scaffolds were subdivided in two printing jobs, 18 scaffolds each. Furthermore, bulk samples have been designed and printed with diameter of 8 mm and height of 8 mm with the purpose to assess the bulk elastic properties (Section 2.4.1).

The stl-file of each of the scaffold structures has been processed and converted to a fab-file format recognized by the 3D-printer in the CeraFab DP (Data Processing, Lithoz Gmbh, Vienna, Austria) software. This software has been used to create the job of the printing machine, to set all the general settings of the process and to adjust the scaffold parameters and their position on the building platform. An important parameter to set is the shrinkage compensation factor to ensure that the final dimensions of the scaffold are close to the programmed ones. Considering the preliminary sintering trials on non-porous specimens, shrinkage compensation factors equal to 1.31 along x/y axes and 1.34 along z axis have been applied in order to oversize the green bodies. The design was adapted in terms of its feature sizes (strut thickness) to be in line with the optical resolution of the specific printer and to compensate for sintering shrinkage. The slurry has been added in the vat of the printer and the building platform has been opportunely prepared. Commercial LithaBone HA480 (Lithoz GmbH, Vienna, Austria) slurry has been used, consisting of powder of HAP homogeneously dispersed with solvent, reactive monomers based on acrylates and methacrylates, a dispersing agent and a photoinitiator. Eighteen scaffolds have been fabricated simultaneously for each printing job using the CeraFab 7500 system (Lithoz GmbH, Vienna, Austria), which is a DLP-based VPP technology using a LED light in the blue visible region as a light source to polymerize the slurry. The DLP printer has a digital mirror device chip as a dynamic mask with a resolution of 1920 × 1080 pixels and pixel size of 40 × 40 μm^2 to expose the image of each layer of the 3D model into photocurable ceramic suspension. When the slurry is exposed selectively and a new layer of the object adheres (or polymerizes) to the building platform (which rises up), the vat rotates to disperse homogeneously the slurry, thus allowing for the next layer to be irradiated and cured until the object is complete. Every single layer has a thickness of 25 μm. After the printing process, the green samples were removed from the building platform and cleaned to eliminate the uncured slurry. Then, all the scaffolds have been thermally treated in the same electrical furnace (Nabertherm P330, Nabertherm GmbH, Germany). Specifically, the thermal post-processing protocol includes the stages of debinding and sintering, with a total treatment time of 122 h and a maximum temperature of 1300 °C maintained for 1 h.

2.2. Phase analysis

One single sample has been pulverized by ball milling (Pulverisette 0, Fritsch GmbH, Germany) and the powders obtained were analyzed by X-ray diffraction (XRD) to identify the crystalline phases. XRD analysis has been performed using the X'Pert Pro PW3040/60 diffractometer (PANalytical, Eindhoven, The Netherlands) in the Bragg–Brentano camera geometry with Cu Kα incident radiation (wavelength λ = 0.15405 nm), filament current 40 mA and voltage 40 kV. Specific experimental parameters of the analysis include 2θ-range of 10° to 70°, angular step size of 0.02° and a counting time of 1 s per step. X'Pert HighScore Software equipped with ICDD PDF (International Centre for Diffraction Data Power Diffraction File) database has been used for the identification of the crystalline phases. For comparative purposes, XRD analysis using the same experimental conditions was also carried out on the as-received ceramic particles embedded in the printable slurry.
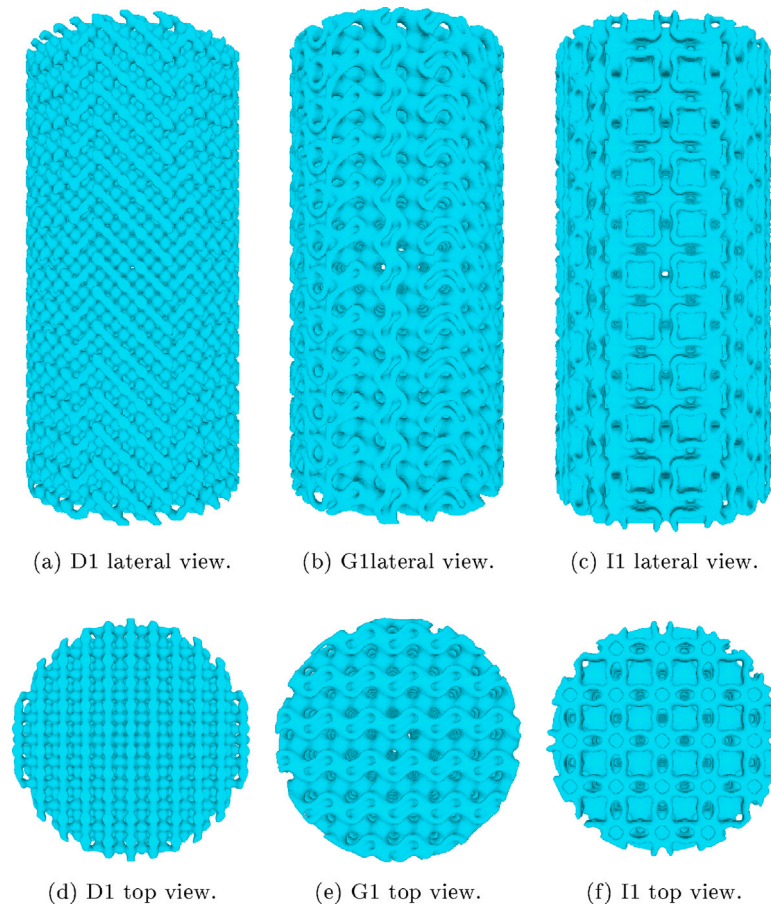
(a) D1 lateral view.   (b) G1lateral view.   (c) I1 lateral view.

(d) D1 top view.   (e) G1 top view.   (f) I1 top view.

Fig. 1. Rendering of the three TPMS geometries characterized in this work, namely Diamond, Gyroid and IWP. The repetitive unit size is such that least 5 cells in the sample diameter were present to guarantee a proper wall spacing.

2.3. Morphological analysis

Computed micro-Tomography (μCT) images have been carried out by using a custom-built equipment manufactured by Fraunhofer-Institut für Keramische Technologien und Systeme (IKTS, Dresden, Germany) featuring an open microfocus X-ray tube and max operating voltage 300 kV. One scan for each type of scaffolds was performed. The acquisition parameters included an acceleration voltage of 100 kV and a current of 120 μA, with a source-to-object distance of 70 mm and a source-to-detector distance of 1400 mm; no filter was used. A rotation step size of 0.225° has been used. The acquisition time for each image was 1 s. For each acquisition, a stack of 16 bit virtual volume of 2024^3 pixels has been obtained, exhibiting a pixel size of 10 μm.

The software Fiji© has been used for image processing [19]. A Gaussian blur of 2 pixels has been used to reduce the noise, and a resampling of 2.5 pixel for each cartesian direction has been used to reduce the overall number of pixels. The image has been rotated firstly manually to align the axis of the cylinder to one of the three cartesian axes, and a further fine alignment has been done by aligning the principal axis of inertia with the cartesian axis through the function *moments of inertia* of BoneJ, plug-in of Fiji© [20]. The wall thickness and the wall spacing have been computed through the same software, using the function *thickness*. The binarization with Otsu algorithm has been applied [21]. The final pixel size of the images is 25 μm. The feasibility of printing process for the TPMS microstructure was verified by comparing the cross section of the printed scaffold obtained through the micro-CT scans and the geometry of the same cross section of the design.

All the samples have been weighted on a scale (resolution 10^{-2} g) and the macroscopic geometrical features measured by a Vernier caliper (overall diameter D and height H) with a resolution of 50 μm. The apparent density (ρ^*) of the samples has been computed as the ratio between the overall mass and the macroscopic volume. The ρ^* found on the non-porous samples, thermally treated under the same conditions used for the TPMS scaffolds, provided the intrinsic density (ρ_0) of HAP. The porosity of the samples has been computed using two different methods. In the first method, the porosity (ϕ^ρ) has been computed as $(\rho_0 - \rho^*)/\rho_0$. The second method is based on the usage of μCT data and the porosity (ϕ^{CT}) has been computed as reported in [22].

Confocal laser images on the lateral side of the cylinders have been acquired (LEXT OLS4100, Olympus, Tokyo, Japan), with 5X magnification, in order to measure the length of the repetitive units. These measurements have been used to determine the wavelength and consequently the frequency to be used for the ultrasound characterization (see Section 2.4.1).

2.4. Mechanical characterization

2.4.1. Elastic properties

The macroscopic elastic properties have been experimentally obtained through the ultrasound method [23]. The samples have been clamped in a suitably designed frame which held the sample in place and aligned with the pulser and the receiver probes (SIUI T5-6L) at the two (top and bottom) faces of the samples. Before sample placement in the holder, the samples have been submerged in a coupling gel (15.140 M.C. matrix couplant, NDT Italiana srl), heated at 70 °C and magnetically stirred until the air bubbles were completely removed from the sample. This procedure was aimed at filling all open porosity of the scaffolds with the gel. Once all air has been removed from the scaffolds, they have been set in the sample holder and submerged in
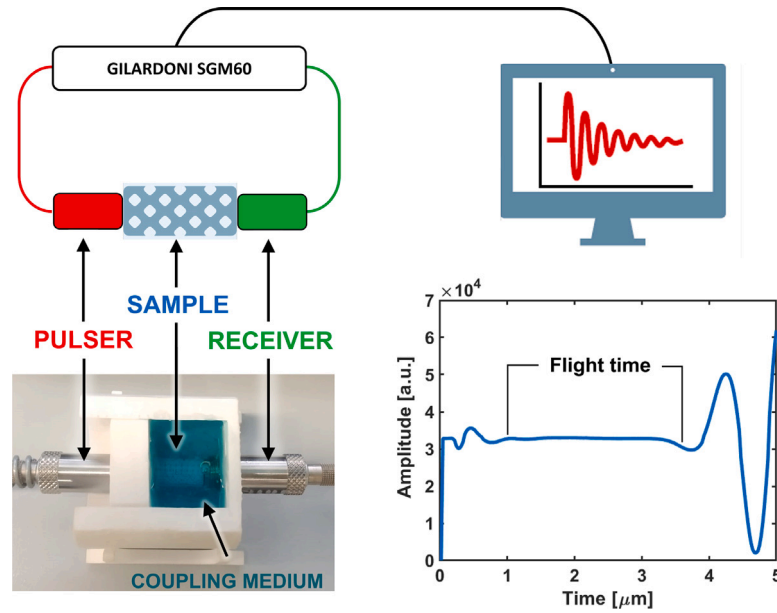
Fig. 2. Schematic representation (top) and real set-up (down) of the experimental ultrasound test and relative outputs. The flight time has been taken according to the standard [24].

the same gel to optimize the transmission of the sound waves through the samples. The ultrasound method determines the elastic properties by measuring the speed of a sound wave, having a suitably selected frequency, through the sample; the wave speed depends on the sample apparent stiffness and apparent density. The experimental set-up and the typical output of the ultrasound investigation is reported in Fig. 2.

A longitudinal ultrasound wave at 1 MHz has been used to fly through the entire length of the scaffold and measure the flight time (Δt). Indeed, a frequency lower than 1.5 MHz was previously identified with the purpose to have a wavelength longer than the size of the unit cell of the scaffold, thus obtaining macroscopic (homogenized) elastic moduli. An ultrasound wave at 5 MHz has been instead used on the bulk sample. The bandwidth at the receiver has been set to 3−7 MHz for the bulk samples and to 0.5−2 MHz for the scaffolds. For both TPMS and bulk samples, Δt has been computed according to the relevant standard [24]. The constrained modulus C_{33} has been determined by means of the model reported in [23]:

$$C_{33} = \rho^* \cdot \left(\frac{H}{\Delta t}\right)^2 \tag{1}$$

The effective elastic modulus along the cylinder's axis ($\bar{E}_z$) has been obtained by assuming the orthotropic material symmetry

$$\bar{E}_z = C_{33} \cdot \frac{(1 - \bar{v}_{xy}\bar{v}_{yx} - \bar{v}_{yz}\bar{v}_{zy} - \bar{v}_{xz}\bar{v}_{zx} - 2\,\bar{v}_{yx}\bar{v}_{zy}\bar{v}_{xz})}{(1 - \bar{v}_{xy}\bar{v}_{yx})} \tag{2}$$

where $\bar{v}_{ij}$ are the macroscopic Poisson's ratios. It is anticipated that the $\bar{v}_{ij}$ have been obtained through the homogenization process, described in Section 2.4.3.

The ultrasound method was also used on bulk samples, where the isotropic material symmetry is assumed:

$$E = C_{33} \cdot \frac{(1 + v)(1 - 2v)}{(1 - v)} \tag{3}$$

where E is the Young's modulus and v the Poisson's coefficient of the bulk HAP. Three porous samples per geometry and three bulk samples have been tested.

2.4.2. Compression strength

Monotonic uniaxial compression tests on the TMPS scaffolds have been run at a controlled displacement rate of 0.5 mm/min until complete failure of the sample. Two stress values have been identified for each test: the first peak at break (exhibiting a stress drop higher than

20% with respect to the highest value, identified as early strength) and the maximum stress obtained during the test (ultimate strength). As the compression tests have been performed on samples with the bulk caps, the assumed gauge length for strain measurement was the distance between the caps (namely the length of the part occupied by the porous micro-architecture). Thirty tests for each class of scaffolds have been performed and the Weibull modulus (m) and the characteristic strength (σ_W) have been computed accordingly [25] for both stresses, i.e. the first peak stress and the maximum stress.

The fracture surfaces of the broken samples have been observed through a confocal laser microscope with a 5X magnification lens to obtain, where possible, a high-resolution quantitative topography of the surface.

2.4.3. Finite element modeling

The elastic properties of the equivalent homogenized material representing the TMPS geometries have been obtained through the numerical homogenization procedure as described in [26]. To this purpose, three cubic domains with an edge length of $D/\sqrt{2}$ (the largest possible) have been cropped from the μCT of each cylinder.

Compression tests with fracture propagation have been simulated to assess the early stage of the fracture pattern on the whole cylinders. Displacement (Dirichlet) boundary conditions have been applied as

$$\begin{cases} u_x|_{\Gamma_B} = 0 \\ u_y|_{\Gamma_B} = 0 \\ u_z|_{\Gamma_B} = 0 \end{cases} \quad ; \quad \begin{cases} u_x|_{\Gamma_T} = -\frac{H}{100} \\ u_y|_{\Gamma_T} = 0 \\ u_z|_{\Gamma_T} = 0 \end{cases} \tag{4}$$

where Γ_B and Γ_T represent the bottom and top surfaces of the cylinder, respectively, simulating a monotonic displacement controlled compression test of samples with the bulk caps. Finite element analyses have been performed by means of the multigrid finite element solver ParOSol [27]. Briefly, the fracture propagation has been modeled by the deletion of the most stressed elements, according to the Drucker–Prager strength criterion [28]. Each element is defined by a hexahedron with 8 nodes (linear shape function for each edge). The material's parameters to feed simulations have been taken from [15], namely $E_0 = 100$ GPa, $v = 0.3$ and $\sigma_0 = 100$ MPa, and already used to model sintered HAP scaffolds [22]. These simulations have been performed on both the μCT-based geometries and on the ideal geometries, since there is a mismatch introduced during the manufacturing process. The effective
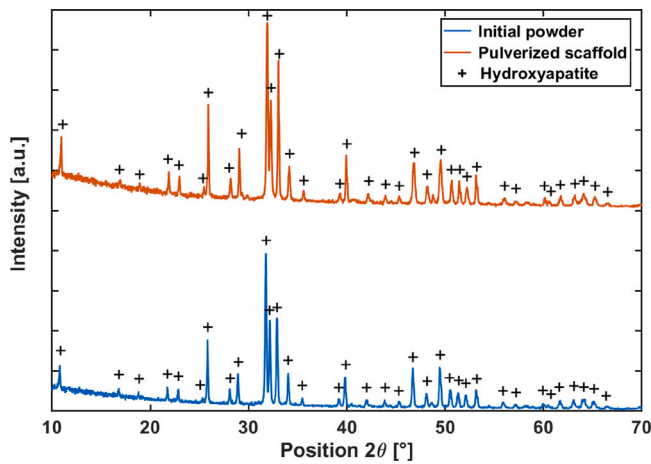
Fig. 3. Comparison of XRD patterns of the initial powder and pulverized scaffold after sintering; the marked peaks correspond to HAP.

stiffness of the scaffold has been evaluated as the slope of the stress–strain graph and the strength as the maximum stress reached by the scaffold during the loading program. The tests were run until a drop of stress of 20% was reached (identified as early strength). The specific strength has been computed by dividing the value of the effective strength by the apparent density of the scaffold ($\rho_0(1-\phi^{CT})$). In order to compare the crack pattern obtained through the finite element models with that shown during the laboratory compression tests, a suitable post-process has been done on the finite element simulation: the elements of the 3D mesh which were subjected to fracture have been eliminated and a connectivity analysis has been performed on the 3D image, in order to isolate the largest connected (not fractured) volume. This procedure will clearly identify the fracture surfaces resulting from the numerical simulations.

3. Results

3.1. Phase analysis

The XRD patterns from the analysis of the initial ceramic powder used in the slurry and the sintered scaffold ground in powder are presented in Fig. 3.

XRD analysis revealed the presence of HAP as the unique crystalline phase, both in the starting powders and in the pulverized scaffolds after sintering, (JCPDS reference code 01-089-6437 in both cases). Neither impurities nor secondary phases are detected after the sintering of the scaffolds, which indicates the thermal stability of the HAP phase. These results are fully consistent with those found by Baino et al. [29] who fabricated HAP foams with bone-like architecture by using the same additive manufacturing technique.

3.2. Morphometric analysis of the 3D printed scaffolds

The bulk samples exhibit a density $\rho_0 = 3.08$ mg/mm^3. Table 1 shows the porosity and the morphometric parameters for the 3D printed scaffolds as measured on the μCT data. The porosity (ϕ^ρ and ϕ^{CT}) for all scaffolds ranges between 43% and 61%; the wall thickness ranges between 277 μm and 439 μm, while the wall spacing ranges between 355 μm and 456 μm. It can be noted that the values of total porosity assessed by mass-volume measurements or tomographic assessment are comparable for the same scaffold type.

Fig. 4 shows the μCT reconstructions and the confocal acquisitions on the lateral surface of the cylinders (scaffolds).

The length of the unit cells ranges from 0.81 mm to 1.61 mm, thereby the frequency for ultrasound investigation has been set to 1 MHz. This

frequency has been verified *a posteriori* considering the velocity of the sound wave in the porous scaffolds, and resulting in a wavelength of 4.88 mm, thereby longer than the repetitive unit and suitable for obtaining the homogenized elastic properties.

Fig. 5 shows a comparison between the design drawing of the IWP structure and the μCT scan of the 3D printed structure. Light blue areas are those of the design, while dark blue color refers to the printed structure. The figure shows how the printed scaffold resulted in a thicker structure, especially in those areas where the design showed thinner walls (thin solid lines represent the boundary of the designed geometry). Similar results have been achieved for the Gyroid and the Diamond geometries. The higher thickness found in some regions of the scaffolds and the clogging of the smallest pores (see the highlighted area on π_2) are responsible for the discrepancy between the designed and the final porosity.

3.3. Mechanical properties

The elastic modulus obtained through the ultrasound method on the bulk samples ranges from 82 GPa to 108 GPa, depending on the Poisson's coefficient (Fig. 6). Considering reliable values of Poisson coefficient (between 0.11 and 0.3) for advanced ceramic materials [30], the value of the Young's modulus is consistent with the results obtained on the same material, measured through nanoindentation and microbending in [15].

The effective (macroscopic) stiffness and strength obtained from the numerical simulations have been reported in Table 2 associated with the measured porosity (ϕ^{CT}). The strength per unit apparent density (specific strength) is also reported in the last column.

The effective (macroscopic) stiffness of the TPMS scaffolds obtained through ultrasound is reported in Table 3 along with the values predicted by the finite element simulations.

Two experimental values of strength are reported in Table 4: the first fracture event (identified as the first stress drop of 20%) and the maximum stress recorded during the whole test. For all scaffolds, the numerically predicted strength falls in the experimental range of the first fracture event; on the contrary, the experimental maximum stress values are higher for all the geometries.

The Weibull plots are reported in Fig. 7. The slope of the linear fitting lines is a graphical representation of the Weibull modulus. It can be seen that the Weibull modulus referred to the ultimate strength is always higher than the Weibull modulus referred to the early strength.

A preferential crack pattern is clearly visible in the Diamond and IWP geometries for both experimental and numerical tests (Fig. 8). Concerning the Diamond structure, the angle between the fracture plane and the load is 35° whereas for the IWP the crack plane is parallel to the load. No preferential crack planes are visible for the Gyroid structure. In scaffolds with Diamond geometry, saddle points on two adjacent planes are shifted so that the line connecting saddle points forms a 35° with the vertical line; this shifting creates the 35° tilting of the fracture plane (see Fig. 8). The same considerations hold for the IWP geometry, where the crack pattern is parallel to the load, and the shifting angle between saddle in adjacent planes is 0°. The absence of preferential crack planes in the Gyroid scaffolds may be due to the skewness of the analytical function generating this TPMS structure.

4. Discussion

The aim of this paper is to assess the mechanical performance of porous HAP scaffolds characterized by three different TPMS architectures, manufactured through VPP and the feasibility of the printing process on complex TPMS structures with micron-size features. To this purpose, HAP cylindrical specimens with Diamond, Gyroid and IWP micro-architectures have been 3D printed. The morphological characterization has been carried out through μCT and confocal microscopy analysis, while mechanical characterization has been carried

Table 1
Morphometric parameters obtained from μCT scans (first column is taken for the sake of comparison).

	Porosity (ϕ^ρ) [%]	Porosity (ϕ^{CT}) [%]	Wall thickness [μm]	Wall spacing [μm]
D1	60.78 ± 0.43	61.39	357 ± 36	424 ± 62
D2	50.96 ± 0.42	53.20	437 ± 42	408 ± 69
G1	58.68 ± 0.49	58.51	319 ± 20	355 ± 56
G2	45.60 ± 0.88	44.54	399 ± 125	456 ± 115
I1	50.91 ± 0.58	48.16	279 ± 43	425 ± 164
I2	43.32 ± 0.97	42.69	317 ± 42	430 ± 188

(a) D1.   (b) G1.   (c) I1.

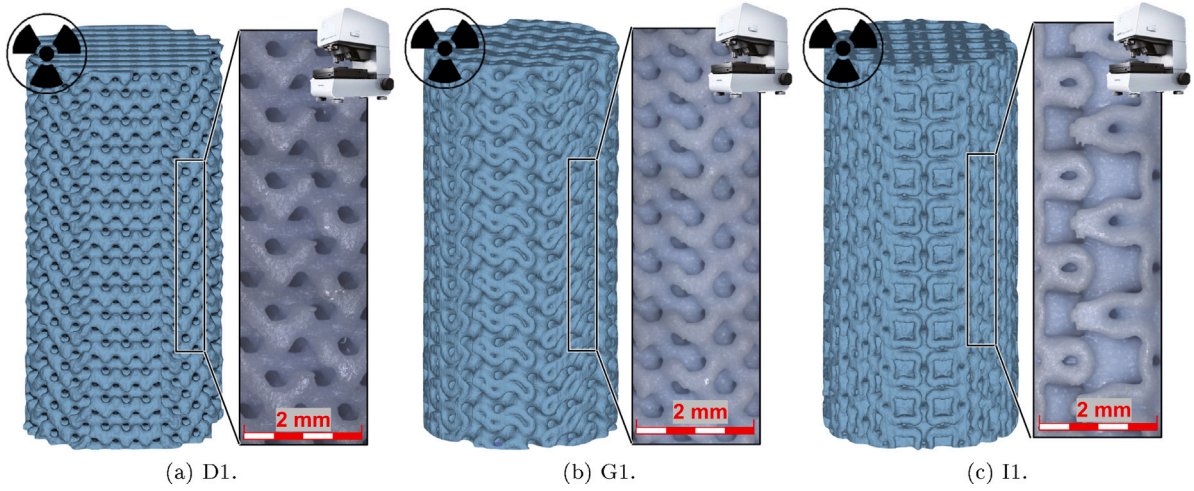**Fig. 4.** μCT reconstruction and confocal laser imaging of the three classes of the scaffolds. The nominal dimensions of the scaffolds are $D = 8$ mm and $H = 16$ mm.
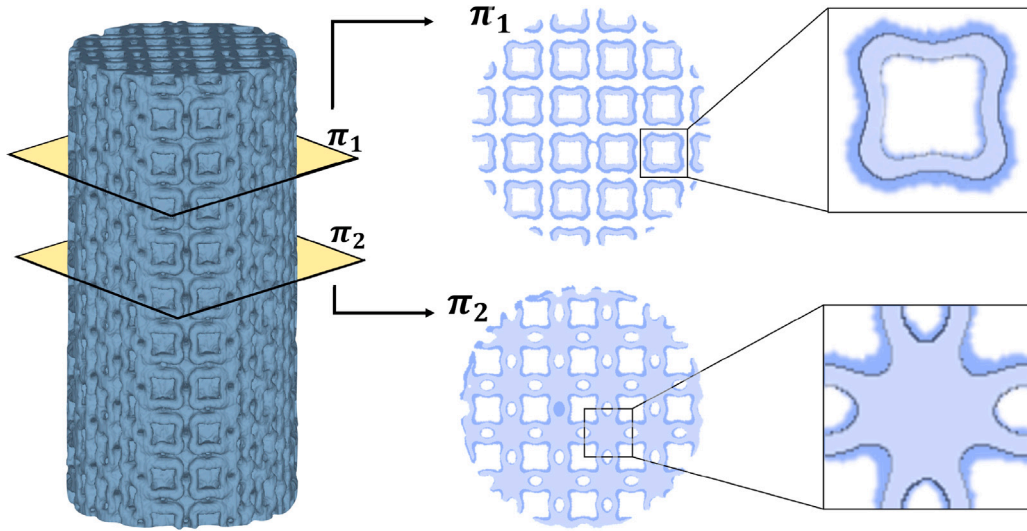

Fig. 5. Rendering of IWP scaffold: on the right two cross sections (planes π_1 and π_2) are reported highlighting the difference between the designed scaffold and the 3D printed one. The over amount of material in the 3D printed scaffold is represented by the dark blue, whereas the black lines denote the designed structure. (For interpretation of the references to color in this figure legend, the reader is referred to the web version of this article.)

Table 2
Morphometric and effective mechanical properties from μCT scans and μCT-based finite element models.

	Porosity (ϕ^{CT}) [%]	Effective stiffness [GPa]	Effective strength [MPa]	Specific strength [J/g]
D1	61.39	10.113	6.364	5.298
D2	53.20	15.214	8.623	5.956
G1	58.51	13.187	9.825	7.418
G2	44.54	26.384	18.234	10.764
I1	48.16	29.325	27.193	16.978
I2	42.69	33.570	31.884	18.161

Table 3

Comparison between the experimental stiffness obtained through ultrasound investigation and the numerical stiffness.

	D1	D2	G1	G2	I1	I2
Exp [GPa]	12.0 ± 0.2	18.9 ± 0.1	14.1 ± 0.6	31.9 ± 0.5	30.2 ± 0.7	32.3 ± 1.1
FEM [GPa]	10.113	15.214	13.187	26.384	29.325	33.570

Table 4

Comparison between the experimental strength obtained through compression tests and the numerical strength. For the experimental data, the average strength, the Weibull modulus (m) and the characteristic strength (σ_W) have been reported.

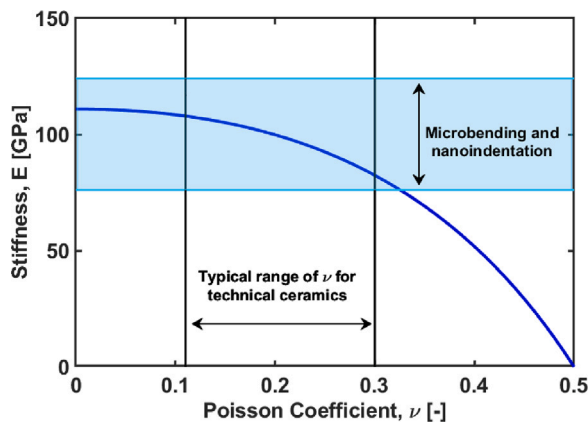|	D1	D2	G1	G2	I1	I2
Exp (ultimate) [MPa]	8.3 ± 1.7	14.3 ± 2.9	17.5 ± 4.1	31.6 ± 7.8	24.9 ± 7.9	35.9 ± 9.0
m (ultimate) [–]	5.4	5.9	4.9	5.4	3.8	4.2
σ_W (ultimate) [MPa]	9.0	15.4	19.0	34.2	27.7	39.6
Exp (early) [MPa]	6.8 ± 2.4	9.9 ± 3.9	13.9 ± 4.5	25.1 ± 7.3	19.8 ± 9.2	31.4 ± 8.4
m (early) [–]	3.2	2.9	3.9	3.8	2.4	4.2
σ_W (early) [MPa]	7.7	11.1	15.4	27.7	22.3	34.6
FEM [MPa]	6.364	8.623	9.825	18.234	27.193	31.884

Fig. 6. Young's modulus E of the bulk hydroxyapatite as a function of ν. The light blue box represents the range of experimental values obtained through microbending and nanoindentation in [15]. The vertical lines represent the minimum and maximum values of ν for advanced ceramics [30]. (For interpretation of the references to color in this figure legend, the reader is referred to the web version of this article.)

out through mechanical laboratory compression tests, ultrasound tests and FEM. No impurities or secondary phases apart from HAP were detected in the scaffolds by XRD analysis (Fig. 3).

With regard to the feasibility of the printing process for these specific structures, in Fig. 5 the worst case among the three geometries is shown in which a reasonably good fidelity of the printing process for the IWP geometry is reported. The mismatch between the design and the printed structure is higher in the area of thinner walls. However, a purposely planned study on a quantitative assessment of the printing fidelity for thin-walled micro-architected structures will be carried out in the future.

Consistently with our study, Hoel et al. [4] also used VPP to produce HAP scaffolds experiencing a reduction of the wall spacing on the 3D printed scaffold with respect to the designed one and an increase of the wall thickness with respect to the target one.

In a related investigation, zirconia scaffolds with three distinct geometries were created using the Nano Particle Jetting™ technique by Cao et al. [31]. The final geometry of the zirconia samples differed from the intended one because the zirconia scaffolds, like HAP scaffolds, were thermally treated after printing. On the other hand, compared to the HAP samples investigated in this paper, there is less mismatch between the designed and printed feature sizes. If a scaling factor was added to the CAD models prior to printing to account for shrinkage brought on by heat treatment, this is not mentioned in the Cao et al. work. It is also important to take into account that zirconia and HAP have distinct thermal shrinkage. Furthermore, the particle size of the

zirconia slurry was smaller than 420 nm, whereas in the present work the particle size of the HAP is around 2 μm ± 0.55 μm; this difference in the particle size may have a significant impact on the final printing fidelity of the scaffolds. Since the two studies deal with different materials and different porosities, a quantitative comparison of the printing feasibility and mechanical properties of HAP scaffolds (present study) and zirconia scaffolds [31] cannot be reliably presented.

In our previous study [15], we have shown that also in the case of simple miniaturized geometry the printed samples exhibited a slightly larger size compared to the nominal dimensions: this is consistent with the findings of the present study. However, in case of more complex design, as in the case of the TPMS architectures, the quantitative assessment of the mismatch is more complex and it goes beyond the aims of this paper. These results indicate that accurate prediction of the shrinkage depending on the characteristic size and on the specific architecture is needed in order to achieve a satisfactory printing fidelity. Concerning the wall spacing and porosity, even if there is a systematic reduction between the designed and 3D printed values, they are still suitable for allowing bone cell colonization [32,33]. Indeed, the morphometric parameters of the 3D printed structures such as overall porosity, wall thickness and wall spacing have a substantial impact on the mechanical response of the devices. Therefore, in this paper an extensive study on the elasticity and strength of VPP-produced HAP structures is carried out by means of ultrasound (for elastic properties) and mechanical compression tests (for the compressive strength). μCT-based FEM have complemented the laboratory tests.

The macroscopic elastic modulus of the TPMS scaffolds ranges between 12 GPa (**D1**) and 32 GPa (**I2**); the numerical prediction of the elastic modulus is consistent with the experimental measurements obtained through the ultrasound method. It is worth noting that the ultrasound technique can provide one single component of the elastic tensor of an anisotropic material, in this case C_{33}, where x_3 is the cartesian direction of the sound wave. The effective elastic modulus ($\bar{E}_z$) along the same direction can be obtained only with an independent estimate of the macroscopic Poisson's ratios ($\bar{\nu}_{ij}$) as reported in Eq. (2). Macroscopic Poisson's ratios are weakly dependent on the Poisson ratio (ν) of the bulk HAP which needs to be assumed. For every geometry in this study, the $\bar{\nu}_{ij}$ have been ascertained using μCT-based FEM. While some researchers have used ultrasound to measure the elastic modulus of scaffolds (see, for instance, [34]), as long as Poisson's ratios are not given, these studies typically only yield partial results.

In this work, the elastic modulus of the scaffolds are experimentally determined using the ultrasound method as we believe that the effective stiffness values found from mechanical compression test are not trustworthy as they are systematically much lower than the expected one (data not shown). A possible reason that explains the mismatch between the effective stiffness of ceramic samples obtained through compression test and ultrasound test may be due to non-idealities
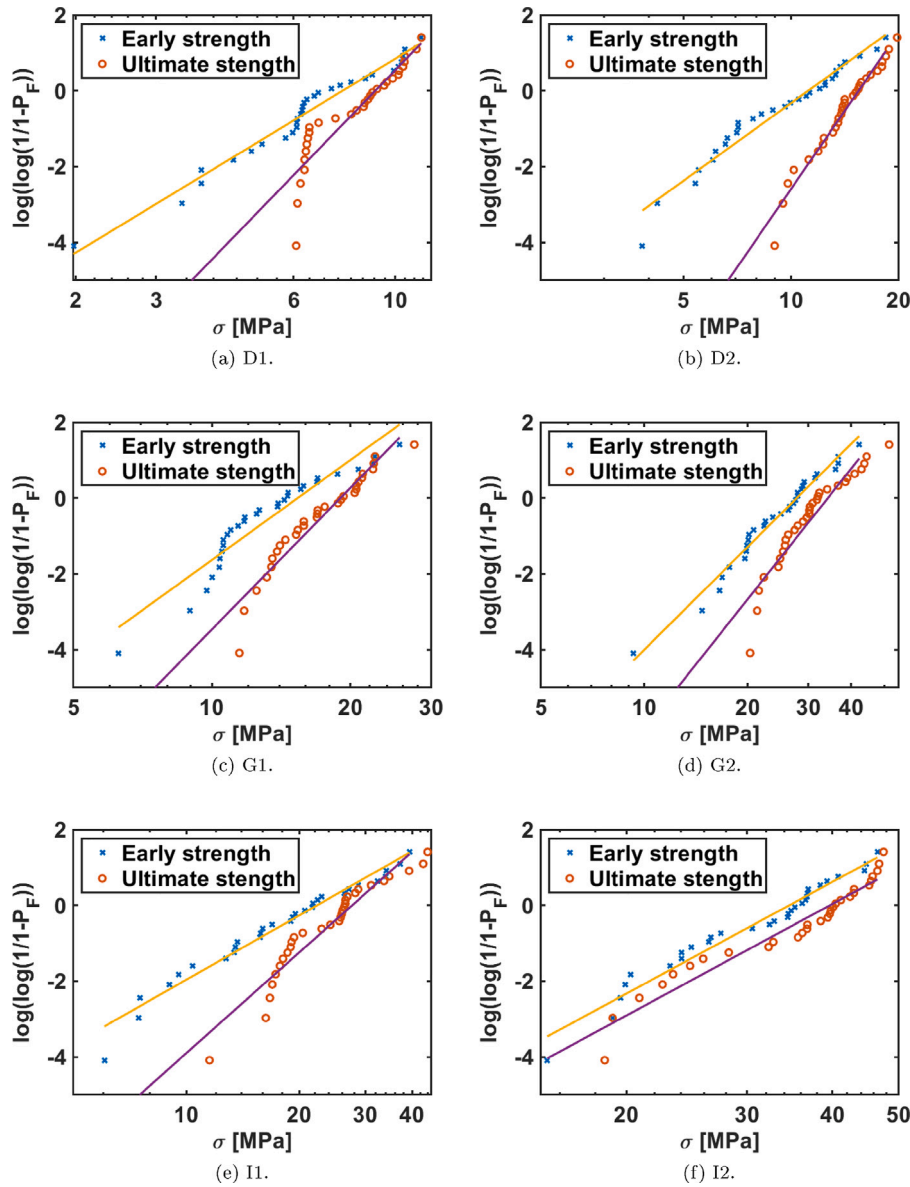
Fig. 7. Weibull plot diagrams obtained from compression tests. All the linear fitting have been performed considering 30 experimental values of strength. The P_F values have been computed as $(j - 0.5)/30$, where j is the ranking number of the scaffold according to its strength [25].

occurring where the boundary conditions are applied during the compression test: in the case of stiff samples (i.e., ceramic samples) the contact between the specimen and the loading nose may be punctual and not uniformly distributed along the two cross sections of the specimen. Although this phenomenon has a substantial impact on the elastic modulus, it does not affect the effective strength (e.g., [29,35–37]). This hypothesis is confirmed by the agreement between the results obtained from ultrasound test and the finite element models. A further validation of the effective stiffness found through ultrasound and FEM is given by the Gibson and Ashby's [38] describing the stiffness-porosity dependence for cellular materials (Fig. 9).

All the geometries tested in this work exhibit elastic moduli significantly higher than those of trabecular bone. However, caution is needed when the effective stiffness of ceramic micro-architectures is compared to the trabecular bone stiffness; indeed, for a clinical application, a more complex device has to be considered, involving also the interaction with the cortical bone [39]. This consideration makes this work a more fundamental study assessing the feasibility of the printing process for complex micro-architected geometries and their relation with mechanical properties.

The early strength of all scaffolds obtained through the finite element models ranges from 6.36 MPa for a Diamond architecture (**D1**) to 31.84 MPa for an IWP (**I2**). These values are consistent with the early strength measured in the compression tests and are always included in the experimental variability. Although less significant from an application perspective, the ultimate strength is slightly less dispersed if compared to the early failure. Indeed, the Weibull parameter *m* for the early failure was lower than that of the ultimate strength, indicating how this property is strongly dependent on the statistical distribution of intrinsic defect (even if not detectable through μCT).

The fracture patterns identified through the numerical simulations are consistent with the ones found in the experiments for the IWP and Diamond architectures. Identifying a clear fracture pattern of compression tests on Gyroid architecture was not possible. The finite element model consistently resulted in a scattered distribution of local cracks. This is likely due to the skewed architecture of Gyroids. A similar scattered pattern of fractures was also found in [31].

The specific strength found in the present study ranged from 6.36 J/g for the **D1** (Diamond) sample to 18.16 J/g for the **I2** (IWP) geometry. These values are in the low range of those found in [31] for zirconia

(a) Post compression sample.

(b) Surface reconstruction.

(c) FEM crack pattern.

(d) Post compression sample.

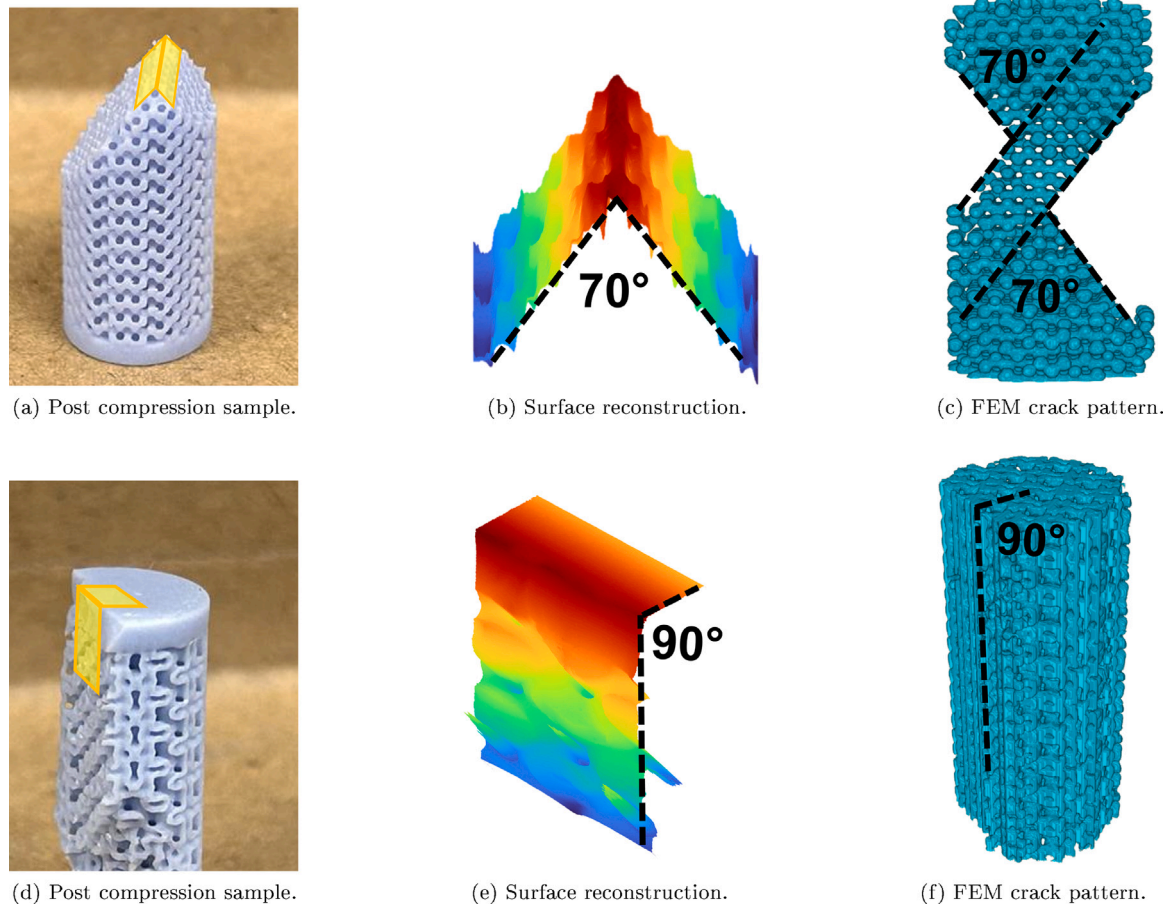(e) Surface reconstruction.

(f) FEM crack pattern.

Fig. 8. Panel (a) and (d): experimental crack pattern obtained from uniaxial compression on a Diamond and a IWP scaffold. Panel (b) and (e): angle of the crack pattern measured through confocal laser imaging on a Diamond and a IWP scaffold, representing the yellow area of panels (a) and (d); the colors represent a height map. Panel (c) and (f): crack pattern obtained through FEM compression test on a Diamond and IWP scaffold. (For interpretation of the references to color in this figure legend, the reader is referred to the web version of this article.)
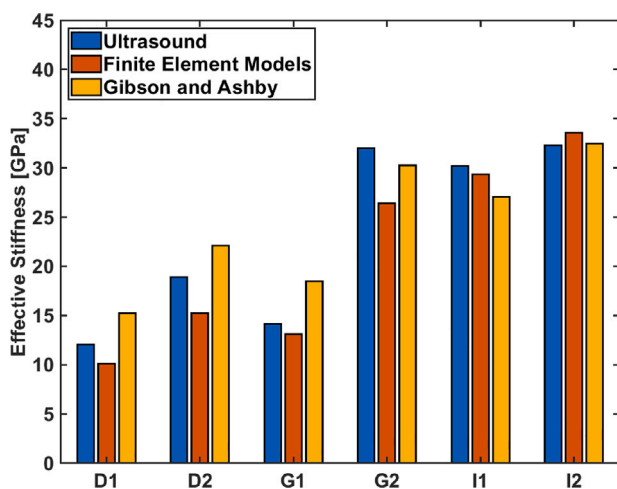

Fig. 9. Comparison between the effective stiffness obtained through ultrasound investigation (3 samples), μCT-based FEM compression tests (1 sample) and the model by Gibson and Ashby [38].

scaffolds; this is justified by the fact that the intrinsic strength of zirconia is substantially higher than that of the HAP bulk material. The lowest specific strength has been found on the Diamond architectures which failed with a 35° inclination of the fracture planes. This suggests

that the Diamond structures are more prone to failure mechanisms activated by the macroscopic shear stress (the maximum shear stress is applied on a plane oriented 45° with respect to the loading direction, i.e. close to the fracture plane orientation). The highest specific strength was found on the IWP architectures which exhibit material continuity along the loading direction; this feature is consistent with a fracture pattern aligned with the loading direction as found in 3D printed grid-like architectures [40–42]. Gyroid structures exhibited an intermediate response. These findings indicate that more extended loading scenarios involving other loading directions with respect to the main architectural orientations are needed for a comprehensive characterization of the scaffold's strength.

The discrepancy between the design and the actual values of the morphologic features (i.e. pore size, porosity or wall thickness) has a substantial impact on the actual value of mechanical properties of the scaffolds in comparison to the predicted ones. Both the stiffness and strength are affected. More in detail, lower porosity with respect to the original design was found for the three geometries, for example, 63% (design) vs. 53% (after sintering) for one of the diamond geometries; or 72% (design) vs. 57% (after sintering) for the one of the gyroid geometries. The smaller porosity obtained in the manufactured samples is mainly due to the higher thickness of the solid walls, as highlighted in Fig. 5. Three main elements determine the final thickness of the solid walls: the shrinkage coefficient applied to the original geometry, the over-polymerization, which could cause pixels next to the image to polymerize, and shrinkage upon debinding and sintering. Conversely to non-porous samples, the exact and simultaneous calibration of all the previously described parameters for architected micro-porous scaffolds
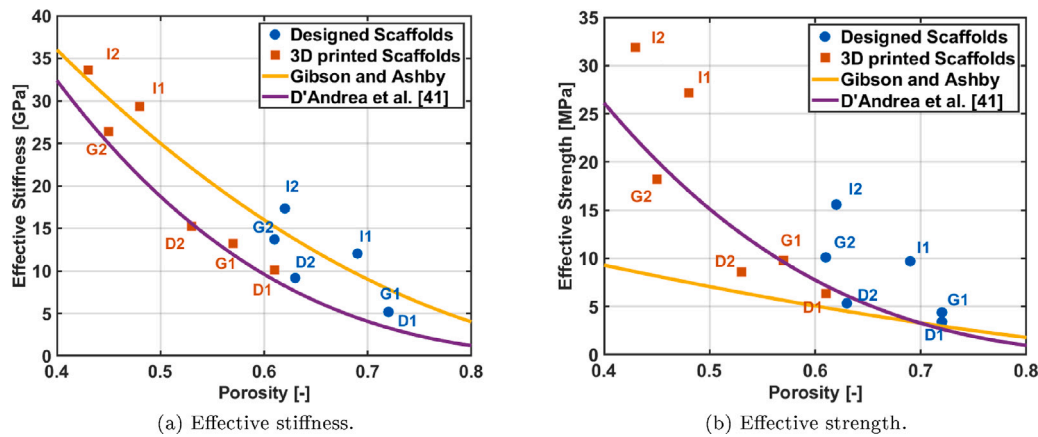
(a) Effective stiffness.

(b) Effective strength.

Fig. 10. Effective stiffness and effective strength of the designed and 3D printed scaffolds obtained through μCT-based FEM, by two analytic models [38,41].

is quite difficult, and can depend greatly on the specific geometry of the microstructures [43].

The values of porosity of designed and printed samples are reported in the abscissa of Fig. 10 which shows the predictions according to the models previously developed by Gibson and Ashby [38] and D'Andrea et al. [41].

Both the analytical models provide a high determination coefficient ($R^2 = 0.95$ and $R^2 = 0.92$ for Gibson and Ashby's and D'Andrea et al.'s models, respectively). Conversely, for the prediction of the effective strength, only the model provided by D'Andrea et al. exhibits a suitable correlation coefficient ($R^2 = 0.93$) as compared to the correlation coefficient of Gibson and Ashby ($R^2 = 0.73$). Indeed, the model by D'Andrea et al. is based on a previous study [28] and incorporates 3D printed ceramic scaffolds, in order to take into account the role of defects occurring during the manufacturing stage, since such defects play a major role in the fracture behavior of the scaffolds.

5. Conclusion

In the current work, three TPMS geometries were considered to fabricate bone tissue engineering HAP scaffolds through VPP. Two main aspects have been considered: (i) the feasibility of the printing process for the sintered scaffolds in comparison to the expected design and (ii) the identification of mechanical properties of 3D printed scaffolds, namely the macroscopic elastic modulus, the compressive strength and the failure mechanisms. μCT scans coupled to finite element simulations allowed us to substantiate the results of this study. The main conclusions can be listed as follows:

– microstructures have been printed with a slight mismatch between the printed and designed geometry that is different in different areas of the scaffolds;
– a small mismatch between the design and the actual geometry has an impact on the mechanical performance; therefore, a quantitative printing fidelity study is necessary;
– the ultrasound technique combined to the numerical homogenization is a suitable experimental tool to obtain the effective stiffness of HAP scaffolds, unlike the compression test;
– the failure mechanisms for Diamond and IWP can be predicted according to geometrical considerations on the locations of the saddle points of the scaffold geometry, while for the Gyroid a clear fracture pattern was not identified due to the skewness of this structure, as per its analytical definition;
– the highest specific strength is found for the IWP geometry, while the lowest one was found for the Diamond architecture;
– failure mechanisms (and fracture patterns) are clearly correlated with the specific strength of the scaffolds.

CRediT authorship contribution statement

Luca D'Andrea: Writing – review & editing, Writing – original draft, Methodology, Investigation. **Roberta Gabrieli:** Writing – review & editing, Writing – original draft, Methodology, Investigation. **Lorenzo Milano:** Investigation. **Luca Magagnin:** Investigation. **Anna De Cet:** Methodology. **Martin Schwentenwein:** Writing – review & editing, Supervision, Investigation. **Enrica Verné:** Writing – review & editing, Writing – original draft, Supervision, Investigation, Conceptualization. **Francesco Baino:** Writing – review & editing, Investigation, Conceptualization. **Pasquale Vena:** Writing – review & editing, Supervision, Methodology, Investigation, Conceptualization.

Ethical issues

None.

Declaration of competing interest

The authors declare that they have no known competing financial interests or personal relationships that could have appeared to influence the work reported in this paper.

Data availability

Data will be made available from the corresponding Author upon reasonable request.

References

[1] A.K. Rajendran, M.S.J. Anthraper, N.S. Hwang, J. Rangasamy, Osteogenesis and angiogenesis promoting bioactive ceramics, Mater. Sci. Eng: R 159 (2024) 100801, http://dx.doi.org/10.1016/j.mser.2024.100801, URL https://www.sciencedirect.com/science/article/pii/S0927796X24000317.

[2] F. Abdollahi, M. Saghatchi, A. Paryab, A.M. Khachatourian, E.D. Stephens, M.S. Toprak, M. Badv, Angiogenesis in bone tissue engineering via ceramic scaffolds: A review of concepts and recent advancements, 2024, http://dx.doi.org/10.1016/j.bioadv.2024.213828.

[3] Y. Cui, S. Hong, W. Jiang, X. Li, X. Zhou, X. He, J. Liu, K. Lin, L. Mao, Engineering mesoporous bioactive glasses for emerging stimuli-responsive drug delivery and theranostic applications, Bioact. Mater. 34 (2024) 436–462, http://dx.doi.org/10.1016/j.bioactmat.2024.01.001, URL https://www.sciencedirect.com/science/article/pii/S2452199X2400001X.

[4] C.A. Hoel, S.K. Peterson, R. Rose, E. Telfeyan, L.A. Boyd, J.H. Her, D.J. Erno, C. Bhushan, J.S. Martinez, B.M. Davis, S. Duclos, G. Parthasarathy, Processing vat polymerized triply periodic minimal surface scaffolds of hydroxyapatite, Adv. Eng. Mater. 25 (2023) http://dx.doi.org/10.1002/adem.202200956.

[5] Y. Zhao, H. Chen, K. Ran, Y. Zhang, H. Pan, J. Shangguan, M. Tong, J. Yang, Q. Yao, H. Xu, Porous hydroxyapatite scaffold orchestrated with bioactive coatings for rapid bone repair, Biomater. Adv. 144 (2023) http://dx.doi.org/10.1016/j.bioadv.2022.213202.

[6] K. Liu, Q. Zhou, X. Zhang, L. Ma, B. Xu, R. He, Morphologies, mechanical and in vitro behaviors of dlp-based 3d printed ha scaffolds with different structural configurations, RSC Adv. 13 (2023) 20830–20838, http://dx.doi.org/10.1039/d3ra03080f.

[7] K. Hayashi, R. Kishida, A. Tsuchiya, K. Ishikawa, Honeycomb blocks composed of carbonate apatite, β-tricalcium phosphate, and hydroxyapatite for bone regeneration: effects of composition on biological responses, Mater. Today Bio. 4 (2019) http://dx.doi.org/10.1016/j.mtbio.2019.100031.

[8] I. Bouakaz, C. Drouet, D. Grossin, E. Cobraiville, G. Nolens, Hydroxyapatite 3d-printed scaffolds with gyroid-triply periodic minimal surface porous structure: Fabrication and an in vivo pilot study in sheep, Acta Biomater. 170 (2023) 580–595, http://dx.doi.org/10.1016/j.actbio.2023.08.041.

[9] S. Systermans, E. Cobraiville, S. Camby, C. Meyer, A. Louvrier, S.A. Lie, T. Schouman, S. Siciliano, O. Beckers, V. Poulet, N. Ullmann, G. Nolens, V. Biscaccianti, J.-L. Nizet, J.-Y. Hascoët, Y. Gilon, L. Vidal, An innovative 3d hydroxyapatite patient-specific implant for maxillofacial bone reconstruction: A case series of 13 patients, J. Cranio- Maxillofac. Surg. (2024) http://dx.doi.org/10.1016/j.jcms.2024.02.026, URL https://linkinghub.elsevier.com/retrieve/pii/S1010518224000738.

[10] L.J. Gibson, M.F. Ashby, Cellular Solids: Structure and Properties, Cambridge University Press, Cambridge, 1997.

[11] H.X. Zhu, J.F. Knott, N.J. Mills, Analysis of the elastic properties of open-cell foams with tetrakaidecahedral cells, 1997.

[12] T.S. Lumpe, T. Stankovic, Exploring the property space of periodic cellular structures based on crystal networks, 2021, 2003504118, http://dx.doi.org/10.1073/pnas.2003504118/-/DCSupplemental, 118.

[13] C. Chatzigeorgiou, B. Piotrowski, Y. Chemisky, P. Laheurte, F. Meraghni, Numerical investigation of the effective mechanical properties and local stress distributions of tpms-based and strut-based lattices for biomedical applications, J. Mech. Behav. Biomed. Mater. 126 (2022) http://dx.doi.org/10.1016/j.jmbbm.2021.105025.

[14] T. Gao, K. Liu, X. Wang, Z. Li, Z. Wang, Elastic mechanical property hybridization of configuration-varying tpms with geometric continuity, Mater. Des. 221 (2022) http://dx.doi.org/10.1016/j.matdes.2022.110995.

[15] L. D'Andrea, D. Gastaldi, F. Baino, E. Verné, G. Saccomano, L. D'Amico, E. Longo, M. Schwentenwein, P. Vena, Mechanical characterization of miniaturized 3d-printed hydroxyapatite parts obtained through vat photopolymerization: an experimental study, J. Mech. Behav. Biomed. Mater. 141 (2023) 105760, http://dx.doi.org/10.1016/j.jmbbm.2023.105760, URL https://linkinghub.elsevier.com/retrieve/pii/S1751616123001133.

[16] L. D'Andrea, A. De Cet, D. Gastaldi, F. Baino, E. Verné, P. Vena, Estimation of elastic modulus, fracture toughness and strength of 47.5b-derived bioactive glass-ceramics for bone scafold applications: a nanoindentation study, Mater. Lett. 335 (2023) 133783, http://dx.doi.org/10.1016/j.matlet.2022.133783, URL https://www.sciencedirect.com/science/article/pii/S0167577X22021383.

[17] S. Ibrahimi, L. D'Andrea, D. Gastaldi, M.W. Rivolta, P. Vena, Machine learning approaches for the design of biomechanically compatible bone tissue engineering scaffolds, Comput. Methods Appl. Mech. Engrg. 423 (2024) 116842, http://dx.doi.org/10.1016/j.cma.2024.116842, URL https://linkinghub.elsevier.com/retrieve/pii/S0045782524000987.

[18] E. Maevskaia, N. Khera, C. Ghayor, I. Bhattacharya, J. Guerrero, F. Nicholls, C. Waldvogel, R. Bärtschi, L. Fritschi, D. Salamon, M. Özcan, P. Malgaroli, D. Seiler, M. de Wild, F.E. Weber, Three-dimensional printed hydroxyapatite bone substitutes designed by a novel periodic minimal surface algorithm are highly osteoconductive, 3D Print. Addit. Manuf. 10 (2023) 905–916, http://dx.doi.org/10.1089/3dp.2022.0134.

[19] J. Schindelin, I. Arganda-Carreras, E. Frise, V. Kaynig, M. Longair, T. Pietzsch, S. Preibisch, C. Rueden, S. Saalfeld, B. Schmid, J.-Y. Tinevez, D.J. White, V. Hartenstein, K. Eliceiri, P. Tomancak, A. Cardona, Fiji: an open-source platform for biological-image analysis, Nature Methods 9 (7) (2012) 676–682, http://dx.doi.org/10.1038/nmeth.2019.

[20] M. Doube, M.M. Klosowski, I. Arganda-Carreras, F.P. Cordelières, R.P. Dougherty, J.S. Jackson, B. Schmid, J.R. Hutchinson, S.J. Shefelbine, Bonej: Free and extensible bone image analysis in imagej, Bone 47 (2010) 1076–1079, http://dx.doi.org/10.1016/j.bone.2010.08.023.

[21] N. Otsu, A threshold selection method from gray-level histograms, IEEE Trans. Syst. Man Cybern. (1979).

[22] L. D'Andrea, D. Gastaldi, F. Baino, E. Verné, M. Schwentenwein, G. Örlygsson, P. Vena, Computational models for the simulation of the elastic and fracture properties of highly porous 3d -printed hydroxyapatite scaffolds, Int. J. Numer. Methods Biomed. Eng. (2023) http://dx.doi.org/10.1002/cnm.3795, URL https://onlinelibrary.wiley.com/doi/10.1002/cnm.3795.

[23] C. Kohlhauser, C. Hellmich, C. Vitale-Brovarone, A.R. Boccaccini, A. Rota, J. Eberhardsteiner, Ultrasonic characterisation of porous biomaterials across different frequencies, Strain (2009).

[24] UNI, Uni en 583-3:1998 non-destructive testing - penetrant testing - part 3: Reference test blocks, 1998.

[25] ASTM, Astm c1239-07 standard practice for reporting uniaxial strength data and estimating weibull distribution parameters for advanced ceramics, 2007.

[26] S.J. Hollister, N. Kikuehi, A comparison of homogenization and standard mechanics analyses for periodic porous composites, Comput. Mech. 10 (1992) 73–95.

[27] C. Flaig, P. Arbenz, A scalable memory efficient multigrid solver for micro-finite element analyses based on ct images, Parallel Comput. 37 (2011) 846–854, http://dx.doi.org/10.1016/j.parco.2011.08.001.

[28] E. Farina, D. Gastaldi, F. Baino, E. Verné, J. Massera, G. Orlygsson, P. Vena, Micro computed tomography based finite element models for elastic and strength properties of 3d printed glass scaffolds, Acta Mech. Sin. 37 (2021) 290–301.

[29] F. Baino, G. Magnaterra, E. Fiume, A. Schiavi, L.P. Tofan, M. Schwentenwein, E. Verné, Digital light processing stereolithography of hydroxyapatite scaffolds with bone-like architecture, permeability, and mechanical properties, J. Am. Ceram. Soc. 105 (2022) 1648–1657, http://dx.doi.org/10.1111/jace.17843.

[30] D. Munz, T. Fett, Ceramics: Mechanical Properties, Failure Behavior, Materials Selection, Springer Series in Materials Science, Berlin, 1999.

[31] E. Cao, Z. Dong, X. Zhang, Z. Zhao, X. Zhao, H. Huang, Mechanical properties and failure analysis of 3d-printing micron-scale ceramic-based triply periodic minimal surface scaffolds under quasi-static-compression and low-speed impact loads, Compos. Sci. Technol. 243 (2023) http://dx.doi.org/10.1016/j.compscitech.2023.110248.

[32] D.J. Lee, J. Kwon, Y.-I. Kim, X. Wang, T.-J. Wu, Y.-T. Lee, S. Kim, P. Miguez, C.-C. Ko, Effect of pore size in bone regeneration using polydopamine-laced hydroxyapatite collagen calcium silicate scaffolds fabricated by 3d mould printing technology, Orthod. Craniofac. Res. 22 (S1) (2019) 127–133, http://dx.doi.org/10.1111/ocr.12261, arXiv:https://onlinelibrary.wiley.com/doi/pdf/10.1111/ocr.12261, URL https://onlinelibrary.wiley.com/doi/abs/10.1111/ocr.12261.

[33] S. Yamahara, J.L. Montenegro Raudales, Y. Akiyama, M. Ito, I. Chimedtseren, Y. Arai, T. Wakita, T. Hiratsuka, K. Miyazawa, S. Goto, M. Honda, Appropriate pore size for bone formation potential of porous collagen type i-based recombinant peptide, Regen. Ther. 21 (2022) 294–306, http://dx.doi.org/10.1016/j.reth.2022.08.001, URL https://www.sciencedirect.com/science/article/pii/S2352320422000797.

[34] D. Bigoni, R. Cavuoto, D. Misseroni, M. Paggi, A. Ruffini, S. Sprio, A. Tampieri, Ceramics with the signature of wood: a mechanical insight, Mater. Today Bio. 5 (2020) http://dx.doi.org/10.1016/j.mtbio.2019.100032.

[35] Y. Li, J. Li, S. Jiang, C. Zhong, C. Zhao, Y. Jiao, J. Shen, H. Chen, M. Ye, J. Zhou, X. Yang, Z. Gou, S. Xu, M. Shen, The design of strut/tpms-based pore geometries in bioceramic scaffolds guiding osteogenesis and angiogenesis in bone regeneration, Mater. Today Bio. 20 (2023) http://dx.doi.org/10.1016/j.mtbio.2023.100667.

[36] C. Polley, T. Distler, C. Scheufler, R. Detsch, H. Lund, A. Springer, D. Schneidereit, O. Friedrich, A.R. Boccaccini, H. Seitz, 3D printing of piezoelectric and bioactive barium titanate-bioactive glass scaffolds for bone tissue engineering, Mater. Today Bio. 21 (2023) http://dx.doi.org/10.1016/j.mtbio.2023.100719.

[37] X. Jiao, F. Wu, X. Yue, J. Yang, Y. Zhang, J. Qiu, X. Ke, X. Sun, L. Zhao, C. Xu, Y. Li, X. Yang, G. Yang, Z. Gou, L. Zhang, New insight into biodegradable macropore filler on tuning mechanical properties and bone tissue ingrowth in sparingly dissolvable bioceramic scaffolds, Mater. Today Bio 24 (2024) http://dx.doi.org/10.1016/j.mtbio.2023.100936.

[38] L.J. Gibson, M.F. Ashby, The mechanics of three-dimensional cellular materials, 1982.

[39] E. Hamed, I. Jasiuk, A. Yoo, Y.H. Lee, T. Liszka, Multi-scale modelling of elastic moduli of trabecular bone, 2012, http://dx.doi.org/10.1098/rsif.2011.0814.

[40] P. Miranda, A. Pajares, E. Saiz, A.P. Tomsia, F. Guiberteau, Fracture modes under uniaxial compression in hydroxyapatite scaffolds fabricated by robocasting, J. Biomed. Mater. Res. A 83A (3) (2007) 646–655, http://dx.doi.org/10.1002/jbm.a.31272, arXiv:https://onlinelibrary.wiley.com/doi/pdf/10.1002/jbm.a.31272, URL https://onlinelibrary.wiley.com/doi/abs/10.1002/jbm.a.31272.

[41] L. D'Andrea, D. Gastaldi, E. Verné, F. Baino, J. Massera, G. Örlygsson, P. Vena, Mechanical properties of robocast glass scaffolds assessed through micro-ct-based finite element models, Materials 15 (2022) 6344, http://dx.doi.org/10.3390/ma15186344, URL https://www.mdpi.com/1996-1944/15/18/6344.

[42] I. Touaiher, M. Saadaoui, P. Reynaud, H. Reveron, J. Chevalier, Mechanical properties of additive-manufactured hydroxyapatite porous scaffolds and follow-up of damage process under compression loading, Open Ceram. 16 (2023) http://dx.doi.org/10.1016/j.oceram.2023.100498.

[43] E. Kornfellner, S. Reininger, S. Geier, M. Schwentenwein, E. Benca, S. Scheiner, F. Moscato, Mechanical properties of additively manufactured lattice structures composed of zirconia and hydroxyapatite ceramics, J. Mech. Behav. Biomed. Mater. 158 (2024) 106644, http://dx.doi.org/10.1016/j.jmbbm.2024.106644, URL https://www.sciencedirect.com/science/article/pii/S1751616124002765.